

## 18. SEDIMENTOLOGICAL AND MINERALOGICAL CONTROL OF MULTISENSOR TRACK DATA AT SITES 981 AND 984<sup>1</sup>

Susan J. Carter<sup>2</sup> and M.E. Raymo<sup>2</sup>

### ABSTRACT

Multisensor track data, including magnetic susceptibility, gamma-ray attenuation porosity evaluator (GRAPE) wet bulk density, and natural gamma emission, were collected on all cores recovered during Ocean Drilling Program Leg 162. Data from the upper Pliocene and lower Pleistocene of Sites 981 and 984 are here compared to results from analyses of a limited set of discrete samples, including benthic foraminiferal isotopic composition, grain size, carbonate content, abundance of foraminifers and lithic particles, and clay mineralogy. Natural gamma emission most closely monitors the input of felsic terrigenous material to these two sites. Magnetic susceptibility also tracks felsic terrigenous input at Site 981 but appears to reflect a separate, more mafic, terrigenous component at Site 984. The GRAPE record does not correlate well with any discretely measured variable at Sites 981 or 984.

### INTRODUCTION

One of the primary objectives of Ocean Drilling Program (ODP) Leg 162 was to investigate the evolution of high-frequency paleoclimatic and paleoceanographic variability in the subarctic North Atlantic. Rapidly accumulated sediments of the Feni, Gardar, and Bjorn Drifts were drilled to recover a record of millions of years of climate history with millennial-scale time resolution. During Leg 162, non-destructive measurements of magnetic susceptibility, natural gamma emission, and gamma-ray attenuation porosity evaluator (GRAPE) wet bulk density data were routinely made on all cores recovered, using the shipboard multisensor track (MST). These three MST data sets were critical stratigraphic tools because they facilitated precise, fast, hole-to-hole correlation and allowed composite sections and splices to be developed at sites with multiple holes, as described in the "Explanatory Notes" chapter of the Leg 162 *Initial Reports* (Shipboard Scientific Party, 1996a).

In addition to their stratigraphic use, MST data from Leg 162 may have great paleoceanographic value. Traditional geochemical and physical measurements done on individual sediment samples to determine past geological or chemical conditions are very labor intensive. The MST data, however, have a sampling density unapproachable by any practical scheme for discrete sampling and are collected on board with minimal effort. Changes in ice rafting on glacial-interglacial and suborbital time scales have been shown to have had a clear impact on the quantity and mineralogy of ice-rafted debris (IRD) in sediments of the North Atlantic over the last glacial cycle (e.g., Ruddiman, 1977; Bond and Lotti, 1995). Because past studies have shown that MST data sets can be useful proxies for sediment source area, transport processes, and local conditions affecting sedimentation, it seems likely that changes in terrigenous input by ice rafting or bottom currents could have distinct signatures in the MST data from Sites 981 and 984. Variation in GRAPE wet bulk density can reflect lithologic variability in sediments that have components of distinctly different grain density or packing efficiency. For example, GRAPE data were used as a proxy for organic carbon content at two Arabian Sea sites (Busch, 1991) and for the relative proportions of opal and carbonate in equatorial Pacific sediments (Mayer, 1991;

Hagelberg et al., 1995). Magnetic susceptibility has been shown to represent the concentration of terrigenous material in sediments, delivered by ice rafting, currents, or ash falls as in the North Atlantic (e.g., Robinson, 1993; Richter et al., 1995), or by wind as in the eastern tropical Atlantic and Indian Oceans (Bloemendal and deMenocal, 1989; deMenocal et al., 1991; Bloemendal et al., 1993). In the North Atlantic, the magnetic susceptibility signal is commonly dominated by the contribution from magnetite, as shown for Site 929 on the Ceara Rise in the western tropical Atlantic (Richter et al., 1997) and for Site 984 (Blum and Richter, 1997). The three common gamma emitters in sedimentary minerals, <sup>232</sup>Th, <sup>238</sup>U, and <sup>40</sup>K, are particularly abundant in material derived from well-differentiated felsic continental rocks, and so natural gamma emission should also reflect the concentration and mineralogy of the terrigenous fraction.

The MST data obtained on sediments from Sites 981 (Feni Drift) and 984 (Bjorn Drift) show clear high-amplitude millennial-scale variability; distinct Milankovitch-scale glacial-interglacial cycles are also visible in data from Site 981. These observations suggest that if the MST records can be calibrated to real sedimentological properties, they may be powerful tools for paleoceanographic interpretation. To relate the Leg 162 MST records to actual sediment lithology and chemistry, a suite of eight samples from Site 981 and 16 samples from Site 984, representative of the full range of MST values over a long time interval, were selected for complete mineralogical and sedimentological analysis. The mineralogy of the clay and fine silt fractions, grain-size distribution, weight percent CaCO<sub>3</sub>, and concentrations of lithic grains and foraminifers were determined for each sample. These results were compared to the MST data and the benthic foraminiferal isotopic records (for 0.9–1.4 Ma only) from each site. R-mode factor analysis helped elucidate the relationships between the discrete variables and the MST data.

### Core Location

Sediment drifts in the far North Atlantic were targeted for drilling during Leg 162 because they record physical and chemical changes in the northern downwelling limb of the global "conveyor belt." High-latitude deep-water formation fills the deep Norwegian-Greenland Seas with dense waters that flow out over parts of the Greenland-Scotland Ridge (GSR). These deep currents have sufficient velocity and sediment supply to maintain a nepheloid layer of fine suspended silt south of the GSR sill (Jones et al., 1970; McCave and Hollister, 1985). Deposition of fine material may occur where the energy of

<sup>1</sup>Raymo, M.E., Jansen, E., Blum, P., and Herbert, T.D. (Eds.), 1999. *Proc. ODP, Sci. Results*, 162: College Station, TX (Ocean Drilling Program).

<sup>2</sup>Dept. of Earth, Atmospheric, and Planetary Sciences, Massachusetts Institute of Technology, Cambridge, MA 02139, U.S.A. scarter@mit.edu

these currents is locally reduced, such as along the boundary of a current or where entrained water reduces the density contrast that drives the current. Because of the large flux of fine material transported in the local nepheloid layers, sedimentation rates are greatly enhanced on the drifts compared with typical pelagic marine sequences. Thus, these drifts record deep circulation in the North Atlantic with unusually high resolution.

Two separate limbs of the deep North Atlantic current system originate at the Wyville-Thomson Ridge (WTR), with a sill depth of ~800 m, and the Iceland-Faeroe Ridge, with a sill depth of ~400 m (Fig. 1). The WTR overflow waters form the sinuous Feni Drift in the southern Rockall Trough (Jones et al., 1970; Robinson and McCave, 1994). Sediment supply to this deep current and its nepheloid layer is from hemipelagic and downslope transport of fine material into upstream areas, in particular from coccolithophorid and other biological productivity in the overlying and upstream waters. Site 981 was drilled on the Feni Drift (55°29'N, 14°39'W, water depth 2200 m; Fig. 1) into sediments consisting of nannofossil ooze with minor components of terrigenous clay, silt and sand, foraminifers, and autochthonous pyritized nodules and burrow casts (Shipboard Scientific Party, 1996b).

West of the Rockall Plateau, on the east flank of the Reykjanes Ridge, deep currents containing dense Iceland-Faeroe Ridge overflow waters deposit the Bjorn Drift. Site 984 was drilled on this drift at 61°26'N, 24°5'W in a water depth of 1650 m (Fig. 1). Unlike those of the Feni Drift, Bjorn Drift sediments are rich in terrigenous silt and clay, derived from Icelandic volcanic material, with relatively minor amounts of nannofossils, foraminifers, biogenic silica, and terrigenous sand. There is also a large and highly variable component of volcanic ash, which may be transported on icebergs or sea ice as well as by wind.

## METHODS

### MST Data

Magnetic susceptibility (MS) is a measure of the ease with which a substance can be magnetized (Robinson, 1993) or, equivalently, the

amount of magnetizable material present. Low-field MS is evaluated by applying a weak magnetic field of known strength to a sample and measuring the strength of the field that results. It is reported as the ratio of the strength of the induced magnetic field to that of the applied field. High concentrations of ferrimagnetic materials, especially magnetite, and also magnetic iron sulfides such as pyrrhotite and greigite lead to high values of low-field MS (Robinson, 1993). Other iron-bearing minerals (such as hematite and goethite) commonly exhibit positive but much weaker MS, whereas pyrite, quartz, and calcite are paramagnetic (characterized by slightly negative MS) (Robinson, 1993). During Leg 162, MS was measured at 3-cm intervals using a Bartington Instruments susceptibility meter with an 80-mm pass-through loop. The resolution of the measurements at Site 981 ranges from ~750 to 300 yr. At Site 984, the MS resolution is ~200–300 yr.

A natural gamma (NG) logger added to the ODP shipboard MST during Leg 149 was extensively used and tested during Leg 150 (Hoppie, 1994). The logger consists of four NaI (thallium activated) scintillation crystals connected to photomultiplier tubes, mounted at 90° to each other in a plane orthogonal to the core track and shielded in a lead housing. A gamma ray hitting one of the scintillation crystals causes the crystal to emit a photon, which the photomultiplier converts to a small current (Bateman, 1985), dependent on the energy of the incident gamma ray. The voltages produced are recorded and stored as a histogram with 2048 energy channels, which are combined for analysis into five energy windows (Hoppie, 1994).

Natural gamma rays were counted for 10 s at 10-cm intervals along nearly every core. All of the NG data were corrected by subtracting from each measurement the average of all of the blanks run during the leg. Although three of the energy windows (channels 3, 4, and 5) were tuned to count geochemically specific peaks, they have never been calibrated, and low numbers of counts resulting from practical limitations to counting time led to poor statistics (Table 1). Therefore, only the counts in the total channel were usable. The resolution of the NG data at Site 981 is between 1000 and 2500 yr, whereas at Site 984, resolution ranges from ~600 to 1000 yr. Although total NG measured on the MST has also not been calibrated geochemically, it should be useful for internally consistent downcore

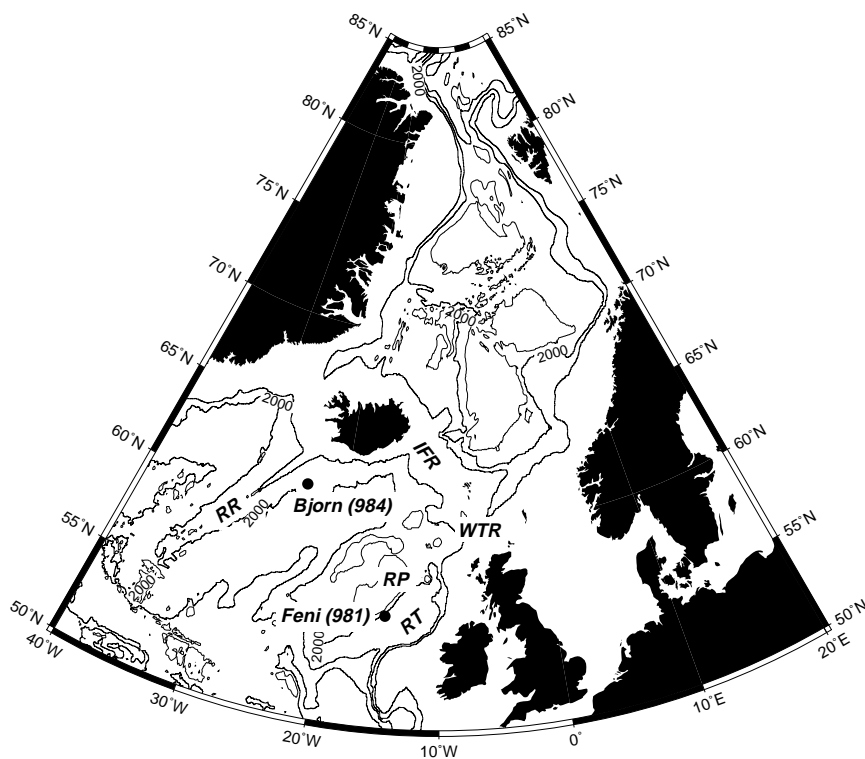


Figure 1. Location map showing Site 981 (Feni Drift) and Site 984 (Bjorn Drift), drilled during Leg 162. IFR = Iceland-Faeroe Ridge, WTR = Wyville-Thomson Ridge, RP = Rockall Plateau, RT = Rockall Trough, RR = Reykjanes Ridge.

**Table 1. Natural gamma emission blank statistics, Leg 162.**

Parameter	Total	Channel 1	Channel 2	Channel 3	Channel 4	Channel 5
Mean counts per second	84.80	46.53	23.16	8.04	2.55	4.53
Standard deviation	9.21	6.82	4.82	2.83	1.60	2.13
Standard deviation (%)	29.33	36.11	47.11	76.18	104.56	101.97

comparisons of the amounts of gamma-emitting minerals present in sediments, similar to the way gamma-ray tools are used in downhole logging to detect clay-rich sequences.

The shipboard MST also includes GRAPE, which is used to measure the wet bulk density of the sediment. The principles and methodology of the GRAPE measurement are discussed in detail by Boyce (1976). Similar to downhole formation density loggers, the GRAPE produces a gamma-ray beam that passes through the core and is attenuated at a rate proportional to the sediment density.

During Leg 162, 2-s GRAPE counts were done, corresponding to a maximum interval of 2 cm. Multiple GRAPE measurements taken at the same depth were averaged, and the data were smoothed with a nine-point Gaussian filter. The few GRAPE wet bulk density values that were  $<1.0$  (pure water) or  $>2.6$  g/cm<sup>3</sup> (pure CaCO<sub>3</sub>) were removed. Unsmoothed GRAPE time resolution is  $\sim 200$ – $500$  yr at Site 981 and between 130 and 200 yr at Site 984, corresponding to a smoothed resolution of  $\sim 800$ – $2000$  yr at Site 981 and 500–800 yr at Site 984. Smoothed GRAPE values were used in all analyses in this study.

A systematic error of  $\sim 10\%$  was found in all the GRAPE measurements from Leg 162 when they were compared with downhole and discrete measurements of wet bulk density. The problem became most obvious when GRAPE measurements made during Leg 162 at revisited Site 907 were compared to the measurements originally made there during Leg 151. The offset was later determined to be due to misalignment of the GRAPE source-sensor apparatus (Shipboard Scientific Party, 1996a). This error was corrected in the data presented here in the following way. For one hole at each site (Holes 981A and 984B), discrete wet bulk density measurements were made gravimetrically on board ship (Shipboard Scientific Party, 1996b, 1996c). Those measurements were compared with the GRAPE values for the exact corresponding depths in those holes. A linear regression was calculated for each site, which was then applied to the spliced GRAPE data as a corrective measure.

Both the raw MS and NG data are dependent on the volume of sediment measured. To normalize both data sets, new GRAPE wet bulk density values were interpolated onto the exact depth vectors for the MS and NG data sets. Dry bulk density was calculated from the GRAPE wet bulk density by assuming a mineral grain density of 2.7 g/cm<sup>3</sup>. The MS and NG values were then divided by the corresponding dry bulk density values. Changes in bulk density were assumed to result only from porosity changes or void space in the core liner. Because void space affects the GRAPE values, normalizing the MS and NG values by dry bulk density calculated from GRAPE corrects in part for water-filled voids. The final data units for each of these data sets are thereby normalized to the mass in grams of solid material in the sediment measured: counts per second (cps) per unit mass for NG and dimensionless units per unit mass for MS. Because the initial measurements were made on ill-defined volumes of sediment, direct conversion to absolute units of mass (e.g., cps/g) was not possible. However, although the units cannot be explicitly stated in either case, they are internally consistent and allow comparison of values both downcore and between sites.

### Discrete Sample Analyses

A total of 16 samples from Site 984 and eight from Site 981 were selected for clay mineralogical analyses. The samples are plotted by depth in meters composite depth (mcd) as solid symbols on Figures 2A, 2B, and 2C (Site 981) and 3A, 3B, and 3C (Site 984). Because of

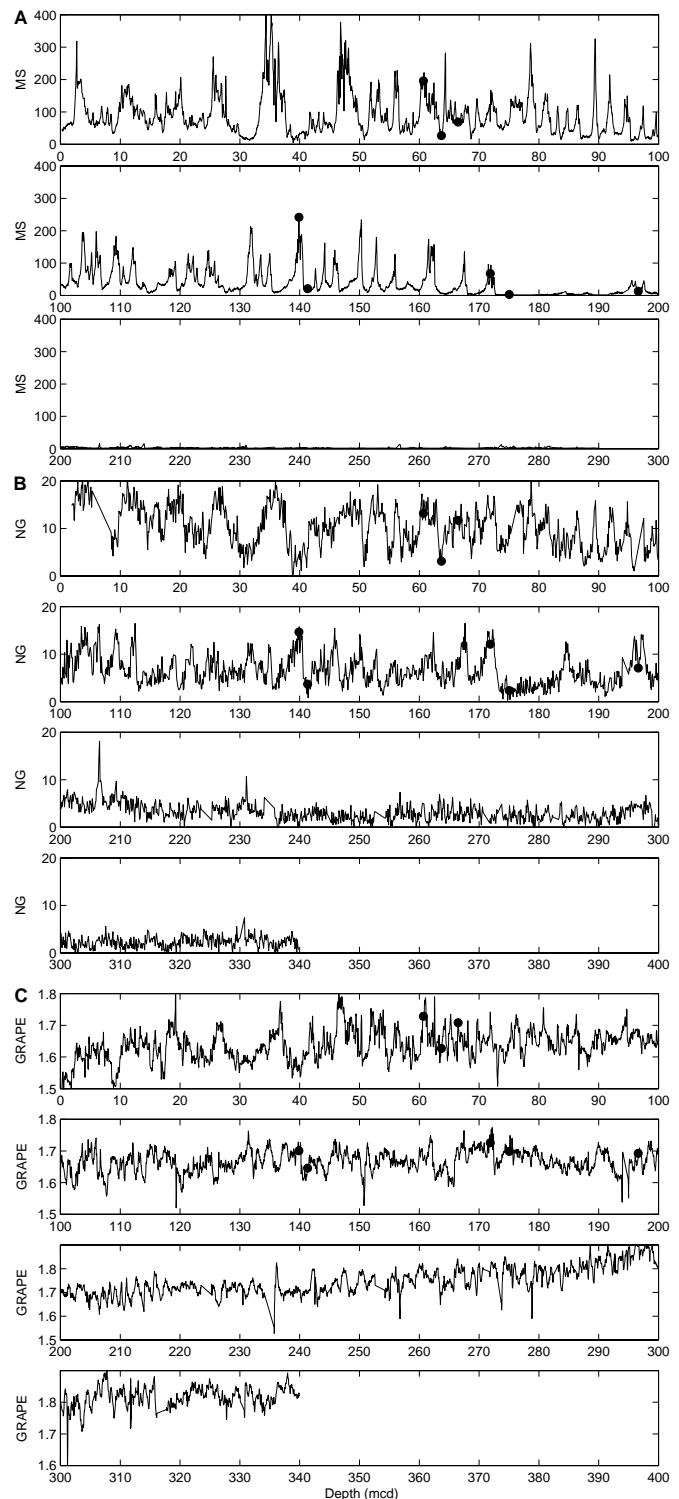


Figure 2. Spliced records from Site 981 (Feni Drift). Discrete sample depths are plotted as solid symbols. **A.** Normalized whole-core magnetic susceptibility. Units are dimensionless magnetic susceptibility units per unit mass. **B.** Normalized whole-core natural gamma emission. Units are gamma counts per second per unit mass. **C.** GRAPE wet bulk density, corrected for source-sensor misalignment. Units are in grams per cubic centimeter.

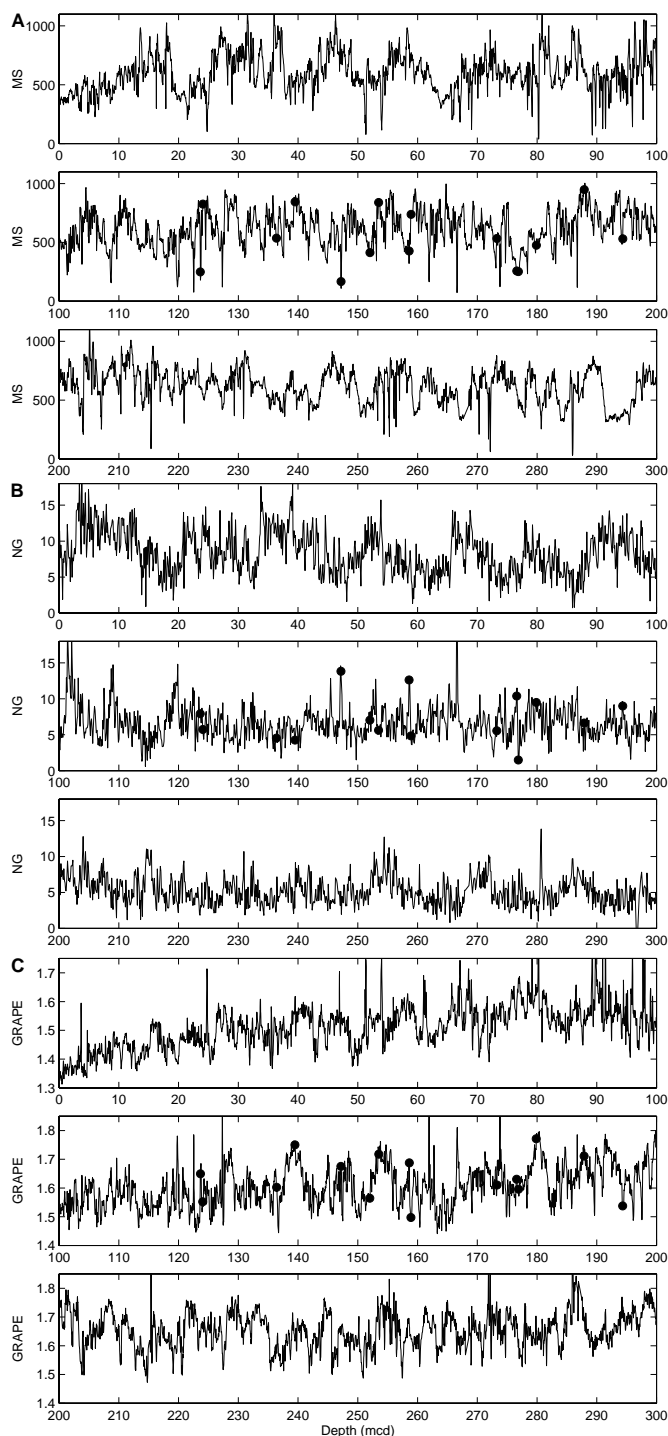


Figure 3. Spliced records from Site 984 (Bjorn Drift). Discrete sample depths are plotted as solid symbols. **A.** Normalized whole-core magnetic susceptibility. Units are dimensionless magnetic susceptibility units per unit mass. **B.** Normalized whole-core natural gamma emission. Units are gamma counts per second per unit mass. **C.** GRAPE wet bulk density, corrected for source-sensor misalignment. Units are in grams per cubic centimeter.

the extremely time-consuming nature of sample preparation for even semiquantitative clay mineralogic analyses by X-ray diffraction (XRD), this subset had to be small. The samples were chosen to span the full range of MS, NG, and GRAPE values at each site.

The clay mineralogy of marine sediments reflects in part the source area of terrigenous material and the climatic conditions that

prevailed there (Griffin et al., 1968). For example, the changing mineralogy of North Pacific sediments has been shown to reflect climatic changes in the eolian source area on Asia (Arnold et al., 1995). Chlorite is one of the initial weathering products of primary continental minerals and is derived from areas where erosion is dominated by mechanical weathering, commonly at high latitudes. Kaolinite, a simple trioctahedral clay from which most of the soluble cations have been removed, occurs toward the other end of the climatic spectrum as a product of severe hydrolysis. Smectite can be an intermediate weathering product, and it is particularly common as an early alteration product of basalts and volcanic ash. Illite is a primary to intermediate weathering product that can be derived from a suite of continental minerals with a chemistry between that of smectite and muscovite, grading into pure fine-grained muscovite. Quartz and plagioclase are primary tectosilicates also present in the clay- and silt-size fractions of deep-sea sediments.

To determine the clay mineralogy and grain-size distribution, we soaked the dry samples overnight in deionized water and then gently sieved them through 63- $\mu\text{m}$ -mesh stainless-steel sieves. The coarse fraction was dry-sieved into 63- to 150- and 150- $\mu\text{m}$  fractions. The fine (<63  $\mu\text{m}$ ) fractions were split using a Honjo wet sample splitter, and a small amount of each was archived. Carbonate was removed from each sample by repeated treatment with buffered acetic acid.

The sedimentology of drift deposits records the physical conditions of their deposition, which are affected by the physical oceanography, geology, and productivity of the region. The grain size of drift material tends to be concentrated in the sortable silt fraction, with the mode of the grain-size distribution controlled by the current speed (McCave et al., 1995). Grain size of current-deposited sediment varies predictably with current strength in the "sortable" range, down to  $\sim 10 \mu\text{m}$  in diameter. Below that, however, particles may behave cohesively, leading to a less straightforward relationship between size distribution and current strength (McCave et al., 1995). Hysteresis between critical velocities for sediment deposition and resuspension, and temporal and spatial variability in current strength, may also complicate interpretation of the grain-size properties of sediments (McCave et al., 1995). In addition, the grain-size distribution of the source material, in particular IRD and biogenic particles, will affect the grain size of a sediment body. Grain-size distributions were measured using the Elzone particle size analyzer at the University of Rhode Island Graduate School of Oceanography (URI-GSO), first on the entire <63- $\mu\text{m}$  size fraction and later on the <20- $\mu\text{m}$  material (separated by wet sieving, using an ultrasonic probe). Results from the two size fractions were graphically "blended" into one continuous grain-size distribution for the <63- $\mu\text{m}$  portion, down to the lower sensitivity limit of the smaller Elzone orifice of  $\sim 2 \mu\text{m}$ . This "blending" combines the two histograms of the coarser and finer ends of the grain-size distribution by scaling the distributions so that the grain counts in the overlapping region (i.e., the channels measured by both orifices) are equal.

To create a constant interlayer spacing and thus a coherent XRD peak for smectite, all <20- $\mu\text{m}$  fractions were treated with 1.0-N  $\text{MgCl}_2$  solution to force Mg into the exchangeable cation sites. The dried <20- $\mu\text{m}$  fraction was then separated into <2- (clay) and 2- to 20- $\mu\text{m}$  (fine silt) fractions by centrifuging. An aliquot of each dried, powdered sample was weighed out and spiked with 10% talc (of the appropriate size fraction) by weight as an internal standard. Sample mounts for XRD were prepared by suspending the sediment in deionized water and then quickly filtering a few milliliters of each sample on 0.45- $\mu\text{m}$  pore-size thin silver foil filters. Air-dried and glycolated samples were X-rayed on the SCINTAG XRD instrument at URI-GSO. Scans from a  $2\theta$  of  $0^\circ$  to  $32^\circ$  allowed smectite, illite, chlorite, kaolinite, quartz, and plagioclase to be distinguished. The near coincidence of the chlorite and kaolinite peaks made it increasingly difficult to resolve the two where the heights of the 3.54- and 3.56- $\text{\AA}$  peaks decreased to  $< \sim 40$  cps. In these instances the peak areas are reported simply as "kaolinite + chlorite." Analytical precision is given in Table 2. These values are derived by comparing the glycolated and

nonglycolated samples for each size fraction at each site, and calculating a mean standard deviation for each as a percent of the mean data value. Anomalous results from the glycolated run of Sample 162-981C-17H-6, 85–87 cm, were not included in the error analysis. The large uncertainty in these results is likely the most significant source of error in the calculated correlations.

Benthic foraminifers, if present, were picked from the >150- $\mu\text{m}$  fraction for isotopic analyses; *Cibicidoides wuellerstorfi* were used where present. Otherwise, other *Cibicidoides* or *Uvigerina* species were used. The samples were split if necessary, and the numbers of foraminifers and of lithic grains per gram of bulk sediment were determined. The number of foraminifers in the >150- $\mu\text{m}$  portion of the coarse fraction, normalized to the original weight of bulk sediment processed, reflects a combination of foraminiferal productivity (relative to delivery of other sediment components) and preservation. Obvious ash particles were not counted as lithic grains; however, rounded to subangular basalt particles were counted. In some cases, there was a continuous gradation from weathered basaltic IRD grains to sharp, fluffy ash shards. Rock fragments and minerals other than quartz and basalt (typically micas or feldspars) were also counted but were rare. Carbonate percentage was determined on archived bulk sample splits using an Ostermann carbonate rig, which reacts each sample with 100% anhydrous phosphoric acid and measures the  $\text{CO}_2$  evolved by pressure transducer.

## RESULTS

### Site 981

#### Isotopes vs. MST Records

Glacial–interglacial changes in sedimentology dominate the MST and the isotope records at Site 981. This interpretation of the long MST records from this site (Fig. 2A, B, C) is supported by visual comparison with the benthic foraminiferal oxygen and carbon isotope data over the interval from 59 to 89 mcd (~0.9–1.4 Ma; Fig. 4). The NG and MS values increase during glacial periods, as indicated by more positive  $\delta^{18}\text{O}$  values, and exhibit features similar to the oxygen isotope record.

To quantify the relationships between these parameters over this interval, we resampled the MST data at the exact depths for which we have isotope data. Because the MS data appear to have a log-normal distribution at Site 981 (unlike all the other data; see Fig. 5), the log of the magnetic susceptibility data (LMS) rather than the raw data are used for the following discussions. Correlations were calculated among the three MST data sets (LMS, NG, and GRAPE) and the two isotope records ( $\delta^{18}\text{O}$  and  $\delta^{13}\text{C}$ ; given in Table 3). F-tests were performed, and only correlations significant at the 95% confidence level are discussed. The correlations given among the MST data are all positive and significant at the 99% level. The LMS and the NG records correlate reasonably well in the interval of 59–89 mcd ( $R = 0.82$ ). Overall, it appears that the components that give the sediment high MS covary with, or are the same as, the components that con-

**Table 2. Analytical precision of XRD measurements, calculated as the percent error.**

Sample size fraction	Total	Illite	Kaolinite + chlorite	Quartz
Site 981				
<2 $\mu\text{m}$	33	37	28	28
2–20 $\mu\text{m}$	18	25	19	14
Site 984				
<2 $\mu\text{m}$	25	*	30	59
2–20 $\mu\text{m}$	37	*	62	34

Note: \*Peak area  $\approx 0$  in many samples; precision poor.

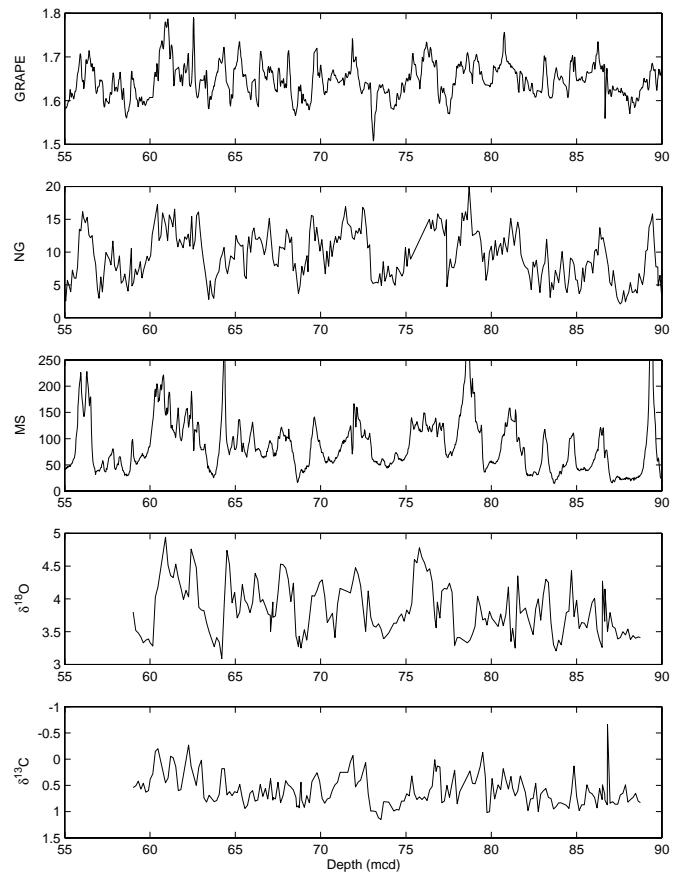


Figure 4. Spliced records of GRAPE wet bulk density, natural gamma emission, magnetic susceptibility, and benthic foraminiferal  $\delta^{18}\text{O}$  and  $\delta^{13}\text{C}$  for the 55–90 mcd (~0.9–1.4 Ma) interval at Site 981. The isotope records are plotted in the opposite of the usual sense to conform visually with the MST records.

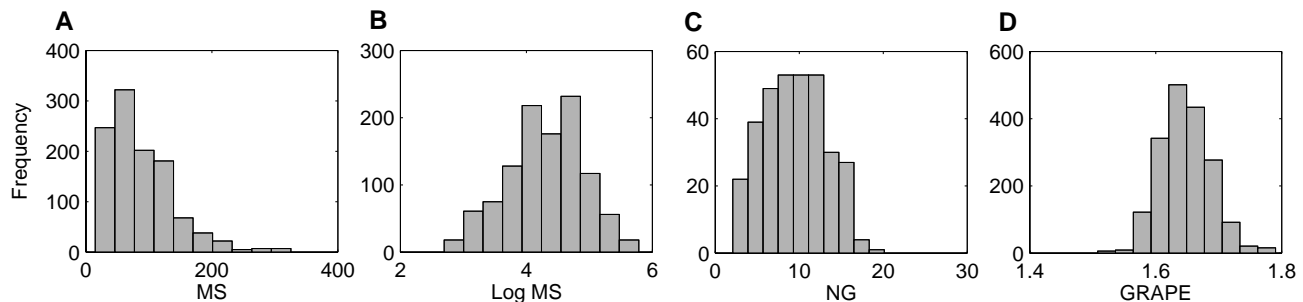


Figure 5. Histograms of MST measurements for the 55–90 mcd interval at Site 981. **A.** Magnetic susceptibility. **B.** Log of magnetic susceptibility. **C.** Natural gamma emission. **D.** GRAPE.

**Table 3. Correlation coefficients (R) for the 0.9–1.4 Ma interval at Site 981.**

Data set	$\delta^{13}\text{C}$	$\delta^{18}\text{O}$	Log MS	GRAPE	NG
$\delta^{13}\text{C}$	1	-0.18	-0.52	-0.35	-0.54
$\delta^{18}\text{O}$		1	0.47	0.31	0.44
Log magnetic susceptibility			1	0.51	0.80
GRAPE wet bulk density				1	0.51
Natural gamma emission					1

Note: Log MS = log magnetic susceptibility, GRAPE = gamma-ray attenuation porosity evaluator, NG = natural gamma.

tribute high NG emission. The GRAPE wet bulk density also tends to increase in concert with MS and NG, which implies that increased abundance of these components reduces the sediment porosity slightly.

There is moderately good correspondence between the benthic  $\delta^{18}\text{O}$  and the NG and LMS records; the correlation is lower but still significant between  $\delta^{18}\text{O}$  and GRAPE. The shapes of the MST and  $\delta^{18}\text{O}$  records are distinctly similar throughout the upper part of this interval (~58–77 mcd): LMS and NG, and to some extent GRAPE, tend to increase within glacial intervals. The similarity between the oxygen isotope record and the MST data appears to deteriorate below ~77 mcd.

Although benthic  $\delta^{13}\text{C}$  and  $\delta^{18}\text{O}$  show only a weak anticorrelation ( $R = -0.18$ ) in the 59–89 mcd interval at Site 981, the  $\delta^{13}\text{C}$  has a stronger anticorrelation with both NG and LMS (-0.55 and -0.52, respectively), showing that the deep water tends to be lighter in  $\delta^{13}\text{C}$  when the delivery or preservation of material with high MS and high NG emission is enhanced. Also, as shown by the positive correlation discussed previously between the benthic oxygen isotope record and these MST parameters, LMS and NG vary with the glacial–interglacial cycles. Therefore, we suggest that some of the variability in the NG emission and LMS data results from glacial–interglacial changes in terrigenous delivery (as shown by the correlation between these data sets and the  $\delta^{18}\text{O}$ ), and some of the variability is associated with changes in deep-water circulation (as shown by the negative correlation between these two MST parameters and the  $\delta^{13}\text{C}$ ). At the most basic level, the correlation with  $\delta^{18}\text{O}$  supports the hypothesis that the long-period variability visible in the MST data is caused by Milankovitch glacial cycles.

### Discrete Sample Analyses

To determine which sedimentological components cause the increase in LMS and NG emission during glacial periods, we compared the MST data to the results of discrete sample analyses (Table 4 [on CD-ROM, back pocket, this volume]). These include clay mineralogy, grain size, and percent calcium carbonate, as well as lithic and foraminiferal counts and isotope data for the subset of eight sediment samples. Statistically significant correlations between MST and discrete data are given in Table 5. Percent carbonate shows a particularly strong negative correlation with both  $\delta^{18}\text{O}$  and NG.

Correlations between these variables are further summarized by R-mode factor analysis of the correlation matrix. Parameters that increase during glacial periods have positive loadings on the first factor (Table 6); strong negative loadings characterize variables that increase during interglacial periods. The glacial–interglacial character of this factor is best demonstrated by its positive association with  $\delta^{18}\text{O}$ . One of the parameters with high negative loading for factor 1 is percent carbonate. This may result from some combination of increased productivity of carbonate-secreting organisms during interglacial periods when iceberg presence is at a minimum and dilution of carbonate material by the increased flux of IRD during glacial episodes.

Many of the sedimentological and mineralogical changes described by the first factor are probably controlled by the delivery of

**Table 5. Statistically significant correlations ( $R^2$ ) between discrete and MST data sets for Site 981.**

Data 1	Data 2	Sign	$R^2$	F-test	
% >63 $\mu\text{m}$	<2 $\mu\text{m}$ , % of <63 $\mu\text{m}$	—	0.55	7.40	
	Elzone mean	+	0.79	22.59	
	<2/2-20 $\mu\text{m}$	—	0.57	7.84	
% carbonate	Clay fraction, total peak area	+	0.56	7.56	
	Quartz (fine silt)	+	0.74	17.03	
	<2 $\mu\text{m}$ , % of <63 $\mu\text{m}$	+	0.61	9.48	
	Benthic $\delta^{13}\text{C}$	+	0.61	9.21	
	Benthic $\delta^{18}\text{O}$	—	0.86	36.20	
	Natural gamma emission	—	0.95	125.31	
2-20 $\mu\text{m}$ , % of <63 $\mu\text{m}$	<2/2-20 $\mu\text{m}$	+	0.51	6.23	
	Total peak area (fine silt)	—	0.62	9.67	
	Kaolinite + chlorite (fine silt)	—	0.67	12.20	
	<2 $\mu\text{m}$ , % of <63 $\mu\text{m}$	—	0.68	13.03	
	Foraminifers/gram	+	0.59	8.59	
	Elzone standard deviation	+	0.73	15.85	
	<2/2-20 $\mu\text{m}$	—	0.83	29.51	
	Total peak area (fine silt)	+	0.76	18.60	
	Benthic $\delta^{18}\text{O}$	—	0.71	14.74	
	Log magnetic susceptibility	—	0.59	8.74	
<2 $\mu\text{m}$ , % of <63 $\mu\text{m}$	Natural gamma emission	—	0.66	11.88	
	<2/2-20 $\mu\text{m}$	+	0.96	143.86	
	Total peak area (clay fraction)	—	0.52	6.47	
	Total peak area (fine silt)	—	0.82	27.31	
	Kaolinite + chlorite (fine silt)	—	0.57	8.11	
	Quartz (fine silt)	—	0.51	6.15	
	Plagioclase (fine silt)	+	0.51	6.27	
	Quartz (fine silt)	+	0.73	16.41	
	<2/2-20 $\mu\text{m}$	—	0.57	7.99	
	Total peak area (fine silt)	+	0.72	15.42	
Benthic $\delta^{13}\text{C}$	Quartz (fine silt)	+	0.66	11.40	
	Benthic $\delta^{18}\text{O}$	—	0.52	6.50	
	Natural gamma emission	—	0.60	9.00	
Benthic $\delta^{18}\text{O}$	Kaolinite + chlorite (fine silt)	—	0.74	16.74	
	Natural gamma emission	+	0.79	22.52	
	<2/2-20 $\mu\text{m}$	—	0.59	8.59	
Log magnetic susceptibility	Total peak area (fine silt)	+	0.57	7.81	
	<2/2-20 $\mu\text{m}$	—	0.55	7.19	
	<2/2-20 $\mu\text{m}$	—	0.57	7.92	
Natural gamma emission	Total peak area (clay)	+	0.64	10.55	
	Total peak area (fine silt)	+	0.70	13.86	
	Kaolinite + chlorite (fine silt)	+	0.78	20.90	
	Quartz (fine silt)	+	0.51	6.21	
	Total peak area (clay)	—	0.53	6.78	
	Total peak area (fine silt)	—	0.88	44.87	
	Kaolinite + chlorite (fine silt)	—	0.51	6.30	
	Quartz (fine silt)	—	0.58	8.18	
	Clay fraction (<2 $\mu\text{m}$ ) XRD	Total peak area	+	0.67	11.99
		Kaolinite + chlorite (fine silt)	+	0.82	28.01
Quartz (fine silt)		+	0.79	22.34	
Illite (clay)		+	0.93	77.13	
Kaolinite + chlorite (clay)		+	0.88	45.95	
Kaolinite (clay)		+	0.90	57.02	
Chlorite (clay)		+	0.87	41.80	
Quartz (clay)		+	0.92	70.78	
Kaolinite + chlorite (clay)		+	0.99	474.66	
Kaolinite (clay)		+	0.97	177.33	
Smectite	Chlorite (clay)	+	0.94	90.61	
	Quartz (clay)	+	0.99	991.60	
	Kaolinite (clay)	+	0.96	142.32	
	Chlorite (clay)	+	0.93	81.43	
	Quartz (clay)	+	0.98	390.72	
	Chlorite (clay)	+	0.99	442.12	
Kaolinite	Quartz (clay)	+	0.98	246.00	
	Quartz (clay)	+	0.96	129.45	
	Quartz (clay)	+	0.96	129.45	
Chlorite	Quartz (clay)	+	0.98	246.00	
	Quartz (clay)	+	0.96	129.45	
	Quartz (clay)	+	0.96	129.45	
Fine silt (2-20 $\mu\text{m}$ ) XRD	Total peak area	+	0.69	13.11	
	Kaolinite + chlorite (fine silt)	+	0.50	6.11	
	Chlorite (fine silt)	+	0.66	11.81	

IRD to the sediments. The mean and standard deviation of the Elzone grain-size distribution are both positively associated with this factor. Because the grain size is measured on the carbonate-free portion of the <63- $\mu\text{m}$  size fraction of the sediment, the variability in the size distribution is caused only by shifts in the source area and transport mechanism of terrigenous sediments and is not affected by changes in carbonate productivity. An increase in the delivery of ice-rafted material to the sediments might be expected to decrease the sorting of the carbonate-free portion and increase the standard deviation of the grain-size distribution. The number of >150- $\mu\text{m}$  lithic particles per gram in these samples, however, has only a weak loading on the first factor, and lithic counts show no statistically significant correlations

**Table 6. First two R-mode factors, Site 981.**

Data set	Factor 1	Factor 2
% >63 $\mu\text{m}$	0.79	0.18
% carbonate	-0.77	-0.09
2-20 $\mu\text{m}$ , % of <63 $\mu\text{m}$	0.73	0.57
<2 $\mu\text{m}$ , % of <63 $\mu\text{m}$	-0.90	-0.34
Foraminifers/gram	0.36	0.52
Lithic grains/gram	0.38	0.53
Elzone geometric mean	0.63	-0.13
Elzone standard deviation	0.69	0.39
$\delta^{13}\text{C}$	-0.75	0.23
$\delta^{18}\text{O}$	0.81	0.02
GRAPE	0.34	-0.24
Log magnetic susceptibility	0.55	0.30
Natural gamma	0.83	0.10
<2/2-20 $\mu\text{m}$	-0.89	-0.42
XRD results, <2 $\mu\text{m}$ (clay fraction)		
Total peak area	0.84	0.09
Smectite	0.66	-0.61
Illite	0.63	-0.73
Kaolinite + chlorite	0.69	-0.70
Kaolinite	0.65	-0.68
Chlorite	0.63	-0.65
Quartz	0.64	-0.71
XRD results, 2-20 $\mu\text{m}$ (fine silt)		
Total peak area	0.90	0.38
Smectite	0.06	0.45
Illite	0.52	-0.22
Kaolinite + chlorite	0.81	0.13
Kaolinite	0.19	-0.10
Chlorite	0.62	0.23
Quartz	0.87	0.05
Plagioclase	0.30	0.48

with any other individual parameter. Therefore, although the supply or absence of IRD may influence the grain size of the sediments deposited at this site, such effects are subtle.

The total XRD peak areas of both the clay and fine silt fractions have strong positive loadings on the first factor. Although peak area is not strictly equivalent to weight percent, changes in the total peak area of the X-ray patterns are representative of changes in the total crystallinity of that fraction of the sediment. Increased delivery of terrigenous material, by ice rafting or by currents, is likely to increase the proportion of well-crystallized material relative to poorly crystalline or amorphous sedimentary components (such as biogenic silica or badly degraded clays) and autochthonous materials, such as iron oxides or organic matter.

The strong associations of the LMS and the NG data with this factor confirm that they are each partially representative of glacial–interglacial changes in sedimentology at this site. The GRAPE wet bulk density also has a positive, although weak, loading on this factor. Examining the long MST records from Site 981 (Fig. 2A), we can see that the MS goes to zero deeper than 173 mcd (at  $\sim 2.7$  Ma, the time of the onset of major Northern Hemisphere glaciation) except for one small pulse at  $\sim 196$ –198 mcd. Sulfate reduction has consumed nearly all of the pore-water sulfate by 150 mcd at Site 981 (Shipboard Scientific Party, 1996b), so it is not unlikely that reduction diagenesis is affecting the MS. Particularly in sediments older than the onset of glaciation, and thus predating any large flux of coarse magnetic material to Site 981, some combination of low supply and diagenesis has produced sediments almost completely void of magnetic material.

Of all the MST data, NG has the clearest association with sediment mineralogy at Site 981, exhibiting a strong negative correlation with weight percent carbonate in the sediment and positive correlations with the total XRD peak areas of the clay and silt fractions and fine-silt kaolinite + chlorite and quartz. The strong negative correlation with carbonate implies that the gamma-emitting material and carbonate are the two most important sedimentary components, and the relative proportions of the two determine the gamma emission of the sediment. Because of the strong correlation of the NG with the oxygen isotope data, we can deduce that terrigenous supply increases, carbonate supply decreases, or both occur during glacial pe-

riods. Neither the grain-size data nor the lithic particle counts identify clearly whether the terrigenous material is primarily IRD or current-deposited silt. However, a moderately strong association of the standard deviation of the grain-size distribution with the first factor shows that sediment sorting is decreased in glacial times. One explanation of this invokes an increased proportion of poorly sorted IRD in the carbonate-free fine fraction. A weak but significant positive association of the lithic counts per gram sediment with factor 1 strengthens the argument that increased IRD delivery is an important part of the glacial–interglacial variability at Site 981, although no significant correlation is evident between lithic counts and  $\delta^{18}\text{O}$  independently.

The second R-mode factor (Table 6) is driven almost entirely by the strong correlation between the clay mineral abundances, particularly in the clay fraction (Table 5). The strong covariation in the clay mineralogy suggests that the source of these clay minerals is relatively constant in its composition. However, the second factor also shows weak loading for the LMS opposite to that of the clay mineral peak areas, which implies that there may be another component contributing slightly to the MS.

In summary, the sediments of Site 981 appear to be primarily a two-component system that varies on glacial–interglacial time scales. Lithic particles from a relatively homogeneous terrestrial source that is characterized by high NG and biogenic carbonates make up most of the sediment. The LMS correlates well with the NG data in the 0.9–1.4 Ma interval, and it has a high loading on the first R-mode factor in the discrete data set, suggesting that it too is controlled in large part by the same terrigenous source.

## Site 984

Unlike at Site 981, where nanofossils make up a large portion of the sediment (Shipboard Scientific Party, 1996b), at Site 984, the abundant sortable silt material is predominantly terrigenous (Shipboard Scientific Party, 1996c). Hence, although biogenic carbonate and IRD are present at both sites, a third independent component of current-transported fine silt with a basaltic composition is also found at Site 984. In addition, there may be a significant fraction of biogenic silica.

### Isotopes vs. MST Records

The MS data at Site 984 appear to be normally distributed (Fig. 6). Visual comparison of the MST data and the stable carbon and oxygen isotopic records of the 0.9–1.4 Ma interval at Site 984 (Fig. 7) shows that the glacial–interglacial contrast characteristic of Site 981 is not as evident at Site 984 (Fig. 3A, B, C). There is a weak positive correlation between the  $\delta^{18}\text{O}$  and MS (Table 7); NG, however, shows no correlation with  $\delta^{18}\text{O}$ . If NG is driven by the relative proportion of terrigenous material as at Site 981, then the input of that material relative to the input of low-NG material is not being paced directly by the Milankovitch-scale glacial–interglacial cycles that control much of the low-frequency oxygen isotope signal. In addition, NG and MS have a weak negative correlation through this interval, which implies that unlike at Site 981, the components controlling these two signals vary independently. Visual inspection of the MST data shows that, although the MS and GRAPE data vary on roughly a glacial–interglacial scale as well as at higher frequencies, the low-frequency band is not apparent in the NG data, although natural gamma data do have a positive correlation with GRAPE data.

### Discrete Samples

A total of 16 samples from Site 984, many of which were barren of benthic foraminifers, were analyzed to help identify the sedimentological variability driving the MST data sets at the Bjorn Drift (Table 8 [on CD-ROM, back pocket, this volume]). Distinct differences

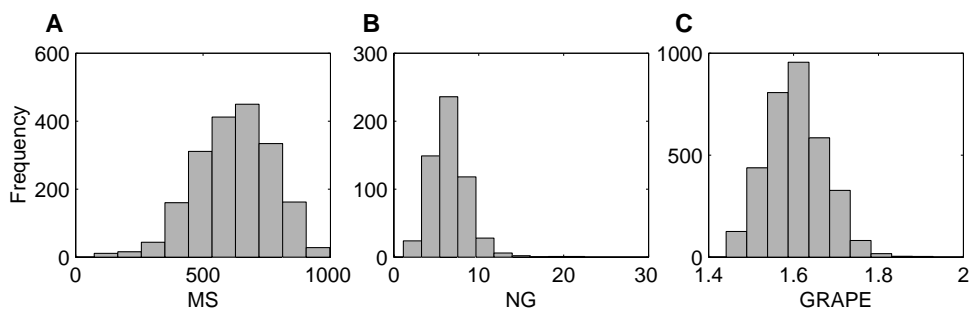


Figure 6. Histograms of MST measurements for the 120–180 mcd interval at Site 984. **A.** Magnetic susceptibility. **B.** Natural gamma emission. **C.** GRAPE.

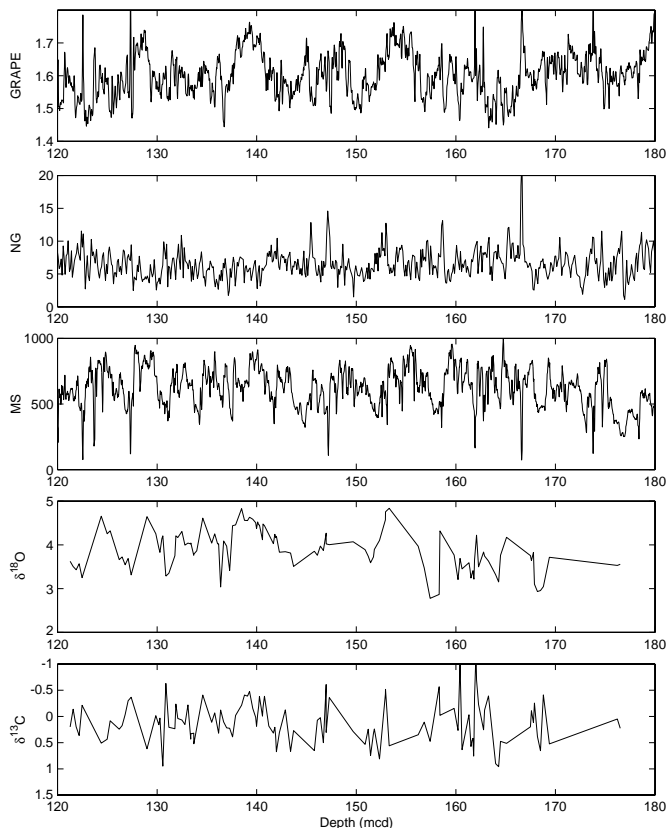


Figure 7. Spliced records of GRAPE wet bulk density, natural gamma emission, magnetic susceptibility, and benthic foraminiferal  $\delta^{18}\text{O}$  and  $\delta^{13}\text{C}$  for the 120–180 mcd (~0.9–1.4 Ma) interval at Site 984. The isotope records are plotted in the opposite of the usual sense to conform visually with MST records.

between Sites 984 and 981 can clearly be seen in comparing the MST and discrete data from the two sites (Tables 9, 10). Although GRAPE values are comparable between the sites, Site 981 has higher NG and Site 984 higher MS values. Compared with Site 981, MS and the number of lithic grains per gram are much higher at Site 984, whereas the NG is distinctly less (Table 10). The mean of the grain size of the carbonate-free <63- $\mu\text{m}$  portion is slightly higher at Site 984, perhaps because of the greater IRD content of the sediments. The standard deviation is the same, however, which implies that the “sortedness” of the terrigenous fraction is about equal at the two sites. The Site 981 sediment is on average nearly 50% carbonate, as opposed to ~7% at Site 984; the counts of foraminifers per gram and the percent coarse fraction also are much higher at Site 981. A comparison of the means of the clay mineralogy data for the two sites (Table 11) shows that the

**Table 7. Correlation coefficients (R) for the 0.9–1.4 Ma interval at Site 984.**

Data set	$\delta^{13}\text{C}$	$\delta^{18}\text{O}$	MS	GRAPE	NG
$\delta^{13}\text{C}$	1	-0.18	-0.01	-0.28	-0.18
$\delta^{18}\text{O}$		1	0.43	0.38	-0.07
Magnetic susceptibility			1	0.13	-0.40
GRAPE wet bulk density				1	-0.15
Natural gamma emission					1

Note: Abbreviations as in Table 3.

**Table 9. Comparison of means between Sites 981 and 984 for MST data, 0.9–1.4 Ma.**

Data set	Site 981		Site 984	
	$\bar{x}$	$\sigma$	$\bar{x}$	$\sigma$
GRAPE wet bulk density	1.647	0.040	1.604	0.068
Magnetic susceptibility	87	52	620	151
Natural gamma	9.45	3.67	6.53	2.21

**Table 10. Comparison of means of discretely measured sedimentology data between Sites 981 and 984.**

Sedimentological data	Site 981 mean	Site 984 mean
% >63 $\mu\text{m}$	8.07	5.94
% carbonate	49.45	7.07
2-20 $\mu\text{m}$ , % of <63 $\mu\text{m}$	41.42	50.12
<2 $\mu\text{m}$ , % of <63 $\mu\text{m}$	26.35	21.44
Foraminifers/g bulk sediment	3305	1460
Lithics/g bulk sediment	96	598
Elzone mean ( $\mu\text{m}$ )	6.98	7.21
Elzone standard deviation	7.80	7.79
GRAPE wet bulk density	1.684	1.626
Magnetic susceptibility	77.1	530.3
Natural gamma emission	8.80	7.31
<2/2-20 $\mu\text{m}$	0.66	0.44

**Table 11. Comparison of means of clay mineralogy data between Sites 981 and 984.**

Mineral	Site 981 mean		Site 984 mean	
	<2 $\mu\text{m}$	2-20 $\mu\text{m}$	<2 $\mu\text{m}$	2-20 $\mu\text{m}$
Total peak area	38,016	20,292	21,610	9,721
Smectite (normalized peak area)	6.99	1.16	4.94	0.69
Illite	1.98	1.16	0.30	0.34
Kaolinite + chlorite	1.39	0.62	0.39	0.18
Kaolinite	0.64	0.44	0.09	0
Chlorite	0.72	0.58	0.14	0
Quartz	2.66	2.41	0.86	0.75
Plagioclase	0	0.43	0.38	0.93

fine, carbonate-free sediment at Site 981 is better crystallized than that at Site 984; the greater total peak area and individual normalized peak areas further suggest that there is a higher concentration of amorphous material (likely biogenic silica) at Site 984.

As at Site 981, correlation between various parameters (Table 12) is summarized by R-mode factor analysis of the data (Table 13). The first factor at Site 984 appears to be representative of IRD input to the sediment, as indicated by its strong positive association with the number of lithic grains per gram. The weight percent in both the clay fraction and the coarse fraction have positive associations with this factor, as does the standard deviation of the grain size. The fine silt fraction, however, shows a strong negative correlation with this factor. Input of poorly sorted IRD may have enhanced the abundances of the coarsest and finest size material at this site. This first factor is strongly associated with the total, illite, kaolinite + chlorite, and quartz XRD peak areas in both the clay and fine-silt size fractions. This implies that IRD input is associated with these primary and secondary minerals that are most likely derived from felsic terrigenous sources. These associations bear up well in the correlations between

the individual data sets (Table 12). In addition, the NG has a positive loading on this factor and correlates well with the XRD peaks of most of the minerals associated with this factor. It appears that the more felsic portion of the IRD input at this site drives the NG signal.

By contrast, smectite and plagioclase do not have strong positive associations with the first R-mode factor. Both size fractions of smectite have only weak loadings for factor 1; the fine silt–fraction plagioclase has a weak negative association. However, the clay-fraction plagioclase has a strong negative association, and the MS also shows a negative loading on this factor. This implies that the sedimentary component associated with clay-fraction plagioclase that contributes the magnetic material is not IRD. Smectite concentration appears to be controlled independently of either the continental IRD or the high-MS source. The only significant correlation that the smectite concentration has is a negative association of the clay-fraction smectite normalized XRD peak area with the Elzone standard deviation. High smectite concentrations therefore are associated with better sorting of the sediments. This suggests that the smectite is delivered primarily by current activity.

**Table 12. Statistically significant correlations ( $R^2$ ) between discrete and MST data sets from Site 984.**

Data 1	Data 2	Sign	$R^2$	F-test				
% >63 $\mu\text{m}$	2-20 $\mu\text{m}$ , % of <63 $\mu\text{m}$	—	0.58	19.27				
	Lithic grains/gram	+	0.56	17.96				
	Magnetic susceptibility <2/2-20 $\mu\text{m}$	+	0.61	21.89				
	Clay fraction, total peak area	+	0.43	10.40				
	Illite (clay fraction)	+	0.29	5.84				
	Plagioclase (clay fraction)	—	0.30	5.89				
	Total peak area (fine silt)	+	0.60	20.58				
	Illite (fine silt)	+	0.29	5.62				
	Illite + chlorite (fine silt)	+	0.34	7.37				
	Quartz (fine silt)	+	0.37	8.26				
	Foraminifers/gram	+	0.31	6.17				
	% carbonate 2-20 $\mu\text{m}$ , % of <63 $\mu\text{m}$	Foraminifers/gram	+	0.65	25.86			
		Lithic grains/gram	—	0.43	10.56			
		Magnetic susceptibility <2/2-20 $\mu\text{m}$	+	0.48	13.02			
Total peak area (clay fraction)		—	0.53	15.51				
Illite (clay fraction)		—	0.45	11.52				
Kaolinite + chlorite (clay)		—	0.44	10.97				
Kaolinite (clay)		—	0.58	19.29				
Chlorite (clay)		—	0.46	12.10				
Quartz (clay)		—	0.44	10.85				
Plagioclase (clay)		+	0.29	5.74				
Total peak area (fine silt)		—	0.39	8.98				
Illite (fine silt)		—	0.61	21.67				
Kaolinite + chlorite (fine silt)		—	0.62	22.65				
<2 $\mu\text{m}$ , % of <63 $\mu\text{m}$		Kaolinite + chlorite (fine silt)	—	0.60	21.02			
	Lithics/gram	+	0.56	18.04				
	Elzone geometric mean	+	0.39	8.91				
	<2/2-20 $\mu\text{m}$	+	0.85	76.44				
	Kaolinite + chlorite (fine silt)	+	0.32	6.63				
	Lithic grains/gram	Magnetic susceptibility <2/2-20 $\mu\text{m}$	—	0.26	4.97			
		Total peak area (clay)	+	0.60	20.79			
		Illite (clay)	+	0.70	32.20			
		Kaolinite + chlorite (clay)	+	0.46	12.01			
		Kaolinite (clay)	+	0.38	8.71			
		Chlorite (clay)	+	0.42	10.34			
		Quartz (clay)	+	0.52	15.01			
		Plagioclase (clay)	—	0.30	5.90			
		Total peak area (fine silt)	—	0.48	12.69			
Illite (fine silt)		+	0.42	10.20				
Kaolinite + chlorite (fine silt)		+	0.34	7.25				
Quartz (fine silt)		+	0.61	21.78				
Elzone geometric mean		—	0.45	11.66				
Elzone standard deviation		—	0.53	15.70				
Magnetic susceptibility	Magnetic susceptibility	—	0.37	8.06				
	Smectite (clay)	—	0.31	6.32				
	Plagioclase (clay)	—	0.33	6.90				
	Illite (fine silt)	+	0.25	4.74				
	Illite (clay)	—	0.32	6.67				
	Kaolinite + chlorite (clay)	—	0.37	8.19				
	Chlorite (clay)	—	0.25	4.73				
	Plagioclase (clay)	+	0.44	11.09				
	Total peak area (fine silt)	—	0.31	6.37				
	Illite (fine silt)	—	0.41	9.76				
	Kaolinite + chlorite (fine silt)	—	0.35	7.47				
	Quartz (fine silt)	—	0.37	8.34				
	Natural gamma emission	Kaolinite + chlorite (clay)	+	0.42	10.21			
		Kaolinite (clay)	+	0.27	5.23			
Illite (fine silt)		+	0.33	6.77				
Total peak area (clay fraction)		+	0.44	11.20				
Illite (clay)		+	0.51	14.47				
Kaolinite + chlorite (clay)		Kaolinite + chlorite (clay)	+	0.26	4.81			
		Kaolinite (clay)	+	0.36	7.93			
		Chlorite (clay)	+	0.34	7.36			
		Quartz (clay)	+	0.30	6.12			
		Total peak area (fine silt)	+	0.50	14.24			
		Illite (fine silt)	+	0.54	16.29			
		Kaolinite + chlorite (fine silt)	+	0.63	24.02			
		Quartz (fine silt)	+	0.44	10.87			
		Clay fraction (<2 $\mu\text{m}$ ) XRD Total peak area	Illite (clay)	+	0.53	16.07		
	Kaolinite + chlorite (clay)		+	0.63	24.21			
	Kaolinite (clay)		+	0.64	24.63			
	Chlorite (clay)		+	0.51	14.86			
	Quartz (clay)		+	0.38	8.43			
	Plagioclase (clay)		—	0.30	5.95			
Total peak area (fine silt)	+		0.62	22.37				
Illite (fine silt)	+		0.42	10.02				
Kaolinite + chlorite (fine silt)	+		0.71	34.09				
Quartz (fine silt)	+		0.56	17.66				
Illite	Kaolinite + chlorite (clay)		+	0.66	26.77			
	Kaolinite (clay)		+	0.37	8.33			
	Chlorite (clay)		+	0.44	10.81			
	Quartz (clay)		+	0.43	10.37			
	Plagioclase (clay)	—	0.34	7.25				
	Total peak area (fine silt)	+	0.77	47.33				
	Illite (fine silt)	+	0.70	32.62				
	Kaolinite + chlorite (fine silt)	+	0.81	59.95				
	Quartz (fine silt)	+	0.82	63.37				
	Kaolinite + chlorite	Kaolinite (clay)	+	0.57	18.29			
		Chlorite (clay)	+	0.58	19.04			
		Quartz (clay)	+	0.35	7.60			
		Plagioclase (clay)	—	0.28	5.32			
		Total peak area (fine silt)	+	0.77	47.26			
Illite (fine silt)		+	0.61	21.75				
Kaolinite + chlorite (fine silt)		+	0.71	35.01				
Quartz (fine silt)		+	0.77	47.90				
Kaolinite		Quartz (clay)	+	0.41	9.82			
		Total peak area (fine silt)	+	0.53	15.77			
		Illite (fine silt)	+	0.37	8.14			
		Kaolinite + chlorite (fine silt)	+	0.52	14.93			
		Quartz (fine silt)	+	0.42	10.06			
		Chlorite	Quartz (clay)	+	0.57	18.21		
	Total peak area (fine silt)		+	0.48	13.15			
	Illite (fine silt)		+	0.31	6.29			
	Kaolinite + chlorite (fine silt)		+	0.50	13.95			
	Quartz (fine silt)		+	0.52	15.39			
	Quartz		Total peak area (fine silt)	+	0.38	8.73		
			Kaolinite + chlorite (fine silt)	+	0.43	10.68		
			Quartz (fine silt)	+	0.42	9.99		
			Total peak area (fine silt)	—	0.27	5.18		
Illite (fine silt)			—	0.34	7.08			
Plagioclase			Kaolinite + chlorite (fine silt)	—	0.37	8.18		
			Quartz (fine silt)	—	0.29	5.61		
			Fine silt (2-20 $\mu\text{m}$ ) XRD Total peak area	Illite (fine silt)	+	0.81	58.51	
				Kaolinite + chlorite (fine silt)	+	0.89	119.20	
		Quartz (fine silt)		+	0.90	122.79		
		Illite		Kaolinite + chlorite (fine silt)	+	0.83	67.91	
				Quartz (fine silt)	+	0.79	53.61	
				Kaolinite + chlorite	Quartz (fine silt)	+	0.88	98.46

**Table 13. First two R-mode factors, Site 984.**

Data set	Factor 1	Factor 2
% >63 $\mu\text{m}$	0.70	-0.36
% carbonate	-0.22	-0.72
2-20 $\mu\text{m}$ , % of <63 $\mu\text{m}$	-0.85	0.18
<2 $\mu\text{m}$ , % of <63 $\mu\text{m}$	0.58	0.53
Foraminifers/gram	-0.24	-0.66
Lithic grains/gram	0.84	0.10
Elzone geometric mean	-0.41	-0.62
Elzone standard deviation	0.36	-0.71
GRAPE	0.24	-0.28
Magnetic susceptibility	-0.67	0.60
Natural gamma	0.48	0.01
<2/2-20 $\mu\text{m}$	0.83	0.31
XRD results, <2 $\mu\text{m}$ (clay fraction)		
Total peak area	0.86	0.21
Smectite	0.03	0.74
Illite	0.89	0.01
Kaolinite + chlorite	0.87	-0.12
Kaolinite	0.81	0.16
Chlorite	0.82	0.08
Quartz	0.70	0.05
Plagioclase	-0.67	0.48
XRD results, 2-20 $\mu\text{m}$ (fine silt)		
Total peak area	0.92	0.04
Smectite	0.24	-0.07
Illite	0.88	-0.12
Kaolinite + chlorite	0.96	0.06
Quartz	0.91	-0.06
Plagioclase	-0.09	0.18

The second R-mode factor at Site 984 emphasizes the correlation between percent carbonate and foraminifers per gram. These two data sets each have strong negative loadings on this factor. Both MS and clay-fraction smectite, however, have positive associations with the second factor. Variation in the relative proportions of biogenic carbonate and magnetic, plagioclase-, and smectite-rich silt components appear to control the second factor.

In summary, four significant sedimentary components appear to influence the MST signals at Site 984. The most distinct component appears to be well-crystallized, poorly sorted, felsic IRD, which correlates strongly with NG. Carbonate is also a distinct, independent component. Third, a plagioclase-rich component that has high MS is associated with good sorting and is probably transported from Iceland as suspended silt in a nepheloid layer; smectite is associated with this material also. As clearly shown by Blum and Richter (1997), the correlation of plagioclase peak area and MS results from the correlation of both variables with magnetite concentration. Biogenic silica probably makes up a fourth component.

## CONCLUSIONS

The high-amplitude variability in the MST data at both Site 984 (Bjorn Drift) and Site 981 (Feni Drift) reflects real changes in sediment properties at those sites. Site 981 appears to be a two-component system, with glacial–interglacial changes in the relative proportion of felsic terrigenous material and biogenic carbonates best represented by NG. The mineralogy of the terrigenous fraction here is relatively constant.

The sedimentology at Site 984 is more complicated than at Site 981. In addition to periodic input of felsic material characterized by high clay mineral abundances and high NG, a major sedimentary component is basaltic material with a low NG but high MS signature transported from Iceland. NG and MS do not appear to vary in concert with each other at Site 984, and we do not observe the relatively simple two-component system seen at Site 981. Instead, there are probably four important independently varying sedimentary components: biogenic carbonate, felsic IRD, mafic terrigenous material derived from Iceland, and a fine amorphous component that may be biogenic silica. Unlike at Site 981, carbonate content and foraminiferal

abundance are low at Site 984 and do not correlate tightly with other sedimentary components.

GRAPE wet bulk density does not correlate particularly well with any sedimentological properties measured at either site, although it clearly increases during glacial intervals at Site 981. One possible unconstrained source of the variance in GRAPE data could be changing biogenic silica content in the sediments. The MST records, in particular MS and NG, appear to be a valuable resource for constructing long, high-resolution records of the concentration of different sedimentary components at Sites 981 and 984.

## ACKNOWLEDGMENTS

We thank Dr. Eve Arnold of URI-GSO for invaluable help with all stages of XRD sample preparation and analysis. S.J. Carter was partially funded by the MIT Joint Program for the Science and Policy of Global Change.

## REFERENCES

- Arnold, E., Leinen, M., and King, J., 1995. Paleoenvironmental variation based on the mineralogy and rock-magnetic properties of sediment from Sites 885 and 886. In Rea, D.K., Basov, I.A., Scholl, D.W., and Allan, J.F. (Eds.), *Proc. ODP, Sci. Results*, 145: College Station, TX (Ocean Drilling Program), 231–245.
- Bateman, R.M., 1985. *Open-Hole Log Analysis and Formation Evaluation*: Boston (Int. Human Resour. Dev. Corp. Press).
- Bloemendal, J., and deMenocal, P., 1989. Evidence for a change in the periodicity of tropical climate cycles at 2.4 Myr from whole-core magnetic susceptibility measurements. *Nature*, 342:897–900.
- Bloemendal, J., King, J.W., Hunt, A., deMenocal, P.B., and Hayashida, A., 1993. Origin of the sedimentary magnetic record at Ocean Drilling Program sites on the Owen Ridge, western Arabian Sea. *J. Geophys. Res.*, 98:4199–4219.
- Blum, P., and Richter, C., 1997. Environmental magnetism of two late Neogene intervals at the Bjorn sediment drift (ODP Site 984), North Atlantic. *Eos*, 78:183.
- Bond, G.C., and Lotti, R., 1995. Iceberg discharges into the North Atlantic on millennial time scales during the last glaciation. *Science*, 276:1005–1010.
- Boyce, R.E., 1976. Definitions and laboratory techniques of compressional sound velocity parameters and wet-water content, wet-bulk density, and porosity parameters by gravimetric and gamma-ray attenuation techniques. In Schlanger, S.O., Jackson, E.D., et al., *Init. Repts. DSDP*, 33: Washington (U.S. Govt. Printing Office), 931–958.
- Busch, W.H., 1991. Analysis of wet-bulk density and sediment color cycles in Pliocene–Pleistocene sediments of the Owen Ridge (Site 722) and Oman Margin (Site 728). In Prell, W.L., Niitsuma, N., et al., *Proc. ODP, Sci. Results*, 117: College Station, TX (Ocean Drilling Program), 239–253.
- deMenocal, P., Bloemendal, J., and King, J., 1991. A rock-magnetic record of monsoonal dust deposition to the Arabian Sea: evidence for a shift in the mode of deposition at 2.4 Ma. In Prell, W.L., Niitsuma, N., et al., *Proc. ODP, Sci. Results*, 117: College Station, TX (Ocean Drilling Program), 389–407.
- Griffin, J.J., Windom, H., and Goldberg, E.D., 1968. The distribution of clay minerals in the World Ocean. *Deep-Sea Res. Part A*, 15:433–459.
- Hagelberg, T.K., Pisias, N.G., Mayer, L.A., Shackleton, N.J., and Mix, A.C., 1995. Spatial and temporal variability of late Neogene equatorial Pacific carbonate: Leg 138. In Pisias, N.G., Mayer, L.A., Janecek, T.R., Palmer-Julson, A., and van Andel, T.H. (Eds.), *Proc. ODP, Sci Results*, 138: College Station, TX (Ocean Drilling Program), 321–336.
- Hoppie, B.W., Blum, P., and the Shipboard Scientific Party, 1994. Natural gamma-ray measurements on ODP cores: introduction to procedures with examples from Leg 150. In Mountain, G.S., Miller, K.G., Blum, P., et al., *Proc. ODP, Init. Repts.*, 150: College Station, TX (Ocean Drilling Program), 51–59.
- Jones, E.J.W., Ewing, M., Ewing, J.I., Eitrem, S.L., 1970. Influences of Norwegian Sea overflow water on sedimentation in the northern north Atlantic and Labrador Sea. *J. Geophys. Res.*, 75:1655–1680.

- Mayer, L.A., 1991. Extraction of high-resolution carbonate data for paleoclimate reconstruction. *Nature*, 352:148–150.
- McCave, I.N., and Hollister, C.D., 1985. Sedimentation under deep-sea current systems: pre-HEBBLE ideas. *Marine Geology*, 66:13–24.
- McCave, I.N., Manighetti, B., and Robinson, S.G., 1995. Sortable silt and fine sediment size/composition slicing: parameters for palaeocurrent speed and palaeoceanography. *Paleoceanography*, 10:593–610.
- Richter, C., Valet, J.-P., Solheid, P.A., 1997. Rock magnetic properties of sediments from Ceara Rise (Site 929): implications for the origin of the magnetic susceptibility signal. In Shackleton, N.J., Curry, W.B., Richter, C., and Bralower, T.J., *Proc. ODP, Sci. Results*, 154: College Station, TX (Ocean Drilling Program), 169–179.
- Robinson, S.G., 1993. Lithostratigraphic applications for magnetic susceptibility logging of deep-sea sediment cores: examples from ODP Leg 115. In Hailwood, E.A., and Kidd, R.B. (Eds.), *High Resolution Stratigraphy*. Geol. Soc. Spec. Publ. London, 70:65–98.
- Robinson, S.G., and McCave, I.N., 1994. Orbital-forcing of bottom-current enhanced sedimentation on Feni Drift, N.E. Atlantic, during the Mid-Pleistocene. *Paleoceanography*, 9:943–972.
- Ruddiman, W.F., 1977. Late Quaternary deposition of ice-rafted sand in the subpolar North Atlantic (Lat 40°N to 65°N). *Geol. Soc. Am. Bull.*, 88:1813–1827.
- Shipboard Scientific Party, 1996a. Explanatory notes. In Jansen, E., Raymo, M.E., Blum, P., et al., *Proc. ODP, Init. Repts.*, 162: College Station, TX (Ocean Drilling Program), 21–45.
- Shipboard Scientific Party, 1996b. Sites 980/981. In Jansen, E., Raymo, M.E., Blum, P., et al., *Proc. ODP, Init. Repts.*, 162: College Station, TX (Ocean Drilling Program), 49–90.
- Shipboard Scientific Party, 1996c. Site 984. In Jansen, E., Raymo, M.E., Blum, P., et al., *Proc. ODP, Init. Repts.*, 162: College Station, TX (Ocean Drilling Program), 169–222.

**Date of initial receipt: 3 September 1997**

**Date of acceptance: 15 July 1998**

**Ms 162SR-022**